**This is the Pre-Published Version.**

This is the peer reviewed version of the following article: L. An, B. Huang, Y. Zhang, R. Wang, N. Zhang, T. Dai, P. Xi, C.-H. Yan, Interfacial Defect Engineering for Improved Portable Zinc–Air Batteries with a Broad Working Temperature. Angew. Chem. Int. Ed. 2019, 58, 9459 - 9463, which has been published in final form at https://doi.org/10.1002/anie.201903879. This article may be used for non-commercial purposes in accordance with Wiley Terms and Conditions for Use of Self-Archived Versions.

# Interfacial Coordinational Coupled Defect Engineering Boosted Portable Zinc-Air Battery with Broad Work Temperature

Li An, Bolong Huang, Yu Zhang, Rui Wang, Nan Zhang, Tengyuan Dai, Pinxian Xi* and Chun-Hua Yan*

**Abstract:** Atomic-thick interfacial dominated bifunctional catalyst NiO/CoO transition interfacial nanowires (TINWs) with abundant coordinational defective sites display high electroactivities and durabilities in the oxygen evolution reaction (OER) and the oxygen reduction reaction (ORR). Density functional theory (DFT) calculations unravel that the excellent OER/ORR performance arises from the electron-rich interfacial region coupled with coordinational defective sites, thus endows the fast redox rate with lower activation barrier for fast electron transfer. When assembled as air-electrode, NiO/CoO TINWs delivered the high specific capacity of 842.58 mAh $g_{Zn}^{-1}$, the large energy density of 996.44 Wh $kg_{Zn}^{-1}$ with long-time stability of more than 33 h (25 °C), and also the superior performance at low (-10 °C) and high temperature (80 °C). Transitional interface engineering open perspectives for rational design advanced oxygen-involved catalysts for wide temperature compatible metal-air batteries.

***H***ighly active energy storage/conversion devices are of great interest owing to their important roles in energy and environmental sustainability.[1] Zn-air batteries (ZABs) with the advantages of high theoretical energy density, low-cost and eco-friendliness are regarded as promising future power devices.[2] However, the electrochemical performance of current ZABs is severely affected by the lack of effective bifunctional catalysts for sluggish oxygen evolution reaction (OER)/oxygen reduction reaction (ORR) at the air-cathode.[3] Although precious Ir/Ru-based or Pt-based materials are commonly regarded as excellent OER or ORR catalysts, electrocatalysts based on non-noble elements are much more desirable for application due to their low-cost and earth-abundance property.[4]

Benefiting from intrinsic corrosion-resistance and cost-efficiency, $NiCo_2O_4$ is particularly advantageous for electrocatalysis and batteries.[5] However, the electrocatalytic performance of $NiCo_2O_4$ structure without further tuning is still inferior to our demands, thus inspiring us to find more effective strategies for structure optimization. As well known, engineering rational interfaces has been considered as an important method to enhance the catalytic performance.[6] Compared with surface sites, stable interfaces with the thickness of 1-2 atoms as dominant sites can avoid the direct contact of the reaction solution. Furthermore, the created interfaces can not only introduce structural discontinuity[7] to promote electronic coupling between adjacent domains[8] but also enrich high-energy defects[9] to enhance catalysis. In addition, interfacial material with greater compositional and structural complexity[10] can exhibit collective properties derived from each fundamental component. However, most of the interface studies are limited to focus on the interaction between different domains while not the interface itself. Above all, establishing an interfacial structure with special spinel $NiCo_2O_4$ as primitive model is crucial for understanding the nature of interface and further designing more ideal nanomaterials.

Herein, we introduce this interfacial effect into the nonprecious Ni-Co-O system via oxygen removing/re-doping strategy. By creating abundant transition interfaces in NiO/CoO transition interfacial nanowires (TINWs), these special interfaces with coordinational defects can be deemed as dominant active sites to accelerate the OER/ORR reaction. As revealed by density functional theory (DFT) calculations, extra high electron-transfer rate originates from the interface region, which induces strong electron-transfer overcoming the Coulomb barrier. This effect is valid through effective *d-d* coupling of Ni-Ni or Co-Co coordinational defects, which further leads to the $e_g$-level close to the Fermi level ($E_F$) for an active $t_{2g}$-$e_g$ electron-transfer. This preliminarily proposed a universal avenue for optimal OER performance, and also favorable for the reversible ORR reaction. Furthermore, the portable ZABs based on atomically-thinned transition interface dominated NiO/CoO TINWs exhibited a high specific capacity of 842.58 mAh $g_{Zn}^{-1}$ and large energy density of 996.44 Wh $kg_{Zn}^{-1}$ at room temperature (25 °C), and also outstanding property at low (-10 °C) and high (80 °C) temperature.

NiO/CoO TINWs were fabricated via oxygen removing/re-doping method using $NiCo_2O_4$ NWs as the precursor. As presented in the X-ray powder diffraction (XRD) patterns in Figure 1a, after the reduction/re-oxidation process, NiO/CoO TINWs with the mixed *cubic* crystal structure of NiO phase (*Fm-3m*; JCPDS: 1-1239) and CoO phase (*Fm-3m*; JCPDS: 1-1227) were prepared from the *cubic* $NiCo_2O_4$. The XRD patterns in Figure S1 verify the complete reduction of $NiCo_2O_4$ NWs to form NiCo alloy, endowing the possibility of atomic coupling interface with transition state by *in-situ* re-oxidation. The almost identical molar ratio values (~1:2) tested by ICP-OES demonstrate that oxygen is the most key factor during the transformation of the initial, reduced, and re-oxidized species (Figure S2). The scanning electron microscopy (SEM) and the transmission electron microscopy (TEM) images illustrate NiO/CoO TINWs and NiCo alloy NWs a much rougher surface with trough-crest configuration compared with the original $NiCo_2O_4$ NWs (Figure S3). Owing to the

[*] L. An, Y. Zhang, R. Wang, N. Zhang, D. Teng, Prof. P. Xi, Prof. C.-H. Yan
State Key Laboratory of Applied Organic Chemistry, Key Laboratory of Nonferrous Metal Chemistry and Resources Utilization of Gansu Province, and College of Chemistry and Chemical Engineering, Lanzhou University, Lanzhou 730000, China
E-mail: xipx@lzu.edu.cn, yan@lzu.edu.cn
B. Huang
Department of Applied Biology and Chemical Technology, The Hong Kong Polytechnic University, Hong Hum, Kowloon, Hong Kong SAR, China
Prof. C.-H. Yan
Beijing National Laboratory for Molecular Sciences, State Key Laboratory of Rare Earth Materials Chemistry and Applications, PKU-HKU Joint Laboratory in Rare Earth Materials and Bioinorganic Chemistry, Peking University, Beijing 100871, China

This article may not be enhanced, enriched or otherwise transformed into a derivative work, without express permission from Wiley or by statutory rights under applicable legislation. Copyright notices must not be removed, obscured or modified. The article must be linked to Wiley's version of record on Wiley Online Library and any embedding, framing or otherwise making available the article or pages thereof by third parties from platforms, services and websites other than Wiley Online Library must be prohibited.

instability under large positive potential in oxygen-involved electrocatalysis, the reduced NiCo alloy is only regarded as intermediate species while not the investigated catalyst. Furthermore, both the Brunauer–Emmett–Teller (BET) theory and the Barrett-Joyner-Halenda (BJH) in Figure S4 indicate NiO/CoO TINWs with larger specific surface area and higher porosity to offer more active sites.[11]

In addition, the high-resolution transmission electron microscopy (HRTEM) results reveal that compared with the $NiCo_2O_4$ NWs, atomic coupling interfaces constructed by two different domains can be easily observed in the NiO/CoO TINWs (Figure S5). To further disclose the interfacial structure of NiO/CoO NWs, atomic-resolution high-angle annular dark-field (HAADF)-aberration corrected scanning transmission electron microscopy (STEM) image was directly performed to analyze the atom arrangements at interface region.[12] The HAADF-STEM and Fast Fourier transform (FFT) images in Figure 1b convincingly manifested the coexistence of two clearly distinct structural domains with the constructed atomic coupling interfaces. FFT-filtered atomic resolution image was further used to visualize the domain transformation (Figure 1c).[13] In addition, eight representative atoms marked as A1, A2, B, C, D1, E1, D2, E2 were selected in the magnified atomic-scale HAADF image (Figure 1d). The corresponding line intensity profiles in Figure 1e directly display the periodic atom arrangements of A1-A2 in the *left* domain and also the D1-E1-D2-E2 periodic atom arrangements in the *right* domain.[14] While the atoms of B and C with irregular profile intensities at the interface region suggest the presence of transition interfacial defects with interfacial electronic coupling. Thus, all the above results verified the successful production of NiO/CoO with abundant transition interfacial defects.

The X-ray absorption near-edge structure (XANES) spectrum at O K-edge was further performed to evaluate the significance of oxygen during the $NiCo_2O_4$-NiO/CoO transformation. As shown in figure 1f, the increased intensity of peak A and the slightly positive shift of peak B suggest the generation of more oxygen deficiencies[15] and charge transfer from the O1s core-state to the *s*, *p*, or *d* hole-states of neighboring atoms[16] over the transition interfaces. The higher photoluminescence (PL) spectra intensity[17] and enhanced electron spin resonance (ESR) signal[18] also suggest the much more oxygen deficiencies on NiO/CoO TINWs, which is demonstrated 2.02 times larger than that of $NiCo_2O_4$ NWs via the X-ray photoelectron spectroscopy (XPS) of O1s peak at 531.4 eV[19] (Figure S6&Table S2). The EXAFS spectra of NiO/CoO TINWs and $NiCo_2O_4$ NWs at Ni/Co K-edge and their corresponding fitting results (Figure S7, S8, S9&Table S3) confirm that the reduction/re-oxidation process weakens the Ni-O and Co-O interaction. Furthermore, the reduced coordination numbers (CNs) and increased disorder degree in the local NiO/CoO TINWs structure with plentiful transition interfaces guarantee their higher activity.[20]

DFT calculation reveals that the transition interface (TI) models of NiO(100) and CoO(111) contains high and low CNs of coordinational defects with (111) and (100) lattice symmetry maintained (Figure 2a). The strain within the CoO TI region leads to an obvious lattice distortion (Figure 2b). The bonding and anti-bonding orbitals near $E_F$ denote the electronically active character within the TI region (Figure 2a&b). For the NiO (TI) model, the projected partial density of states (PDOSs) shows the broadened bands of both Ni-3d and O-2p, compared to the original surfaces. The $t_{2g}$-$e_g$ splitting effects have been substantially narrowed within the TI region (Figure 2c). The TI contributes similarly to modulating the 3d-bands of Ni- and Co-sites from NiO (TI) and CoO (TI) systems, respectively. The electron-rich Co-3d bands display wider *p*-*d* overlapping for better site-to-site electron-transfer (Figure 2d). The IF induces strong electron-transfer overcoming the Coulomb barrier that is valid through effective *d*-*d* coupling of Ni-Ni or Co-Co coordinational defects, which further leads to an active $t_{2g}$-$e_g$ electron-transfer (Figure 2e). Detailed site-dependent analysis of TI region in NiO (TI) system from (100) and (111) shows that, compared to the regions with distance from TI, the Ni-3d bands near TI region exhibit high electronic activities staying close to $E_F$ with nearly diminished $e_g$-feature (Figure S10a&b). Moreover, further closer viewing of Ni-bands also presents a finely modulated peak positions for better selectivity of electron-transfer from the site-to-site perspective (Figure S10c). Meanwhile, a similar electronic trend of site-dependent Co-3d band in the CoO (TI) system is noted. In addition, the TI region broadens the Co-3d bands to be an electron-rich character. Such trend further exhibits higher activities for electron-transfer as the $t_{2g}$-$e_g$ gap is minimized as $e_g$ state obviously across $E_F$ (Figure S10d).

The OER and ORR properties of these catalysts were further evaluated in 1.0 M KOH solution. NiO/CoO TINWs possess the best OER property with the low overpotential ($\eta$ = 255 mV at $j$ = 10 mA $cm^{-2}$) and excellent ORR ability with the onset potential of 0.908 V and half-wave potential ($E_{1/2}$) of 0.818 V (Figure S11). In addition, after surface area normalization via BET, the superiority of NiO/CoO TINWs is still remarkable, which further demonstrates their enhanced intrinsic activity owing to the formation of transition coupling interfaces (Figure S12).[21] Furthermore, NiO/CoO TINWs show high stability with a slight current attenuation of 0.3% after 20 h OER running (Figure S13) and only 2.6% current density loss after 20 h ORR testing (Figure S14). Importantly, NiO/CoO TINWs exhibit an outstanding overall electrode performance with the lowest $\Delta E$ (0.682 V) (Figure 3a&Table S4). As shown in Figure 3b, NiO/CoO TINWs was further used as air-cathode of primary ZABs with 6.0 M KOH aqueous as the electrolyte.[22] This primary ZAB with large open-circuit voltage (OCV = 1.492 V, Figure S15) deliver the maximum power density of about 151 mW $cm^{-2}$, larger than $NiCo_2O_4$ NWs (67 mW $cm^{-2}$) and Pt/C + $IrO_2$ (112 mW $cm^{-2}$). After further adding 0.2 M zinc acetate into electrolyte, the corresponding rechargeable ZAB was constructed, which can continuously keep working for about 332 h via mechanically replenishing Zn plate for four times (Figure S16) without obvious change on the morphology and structure of NiO/CoO TINWs (Figure S17), indicating its structural stability in the long cycling life ZABs configuration.

To explore the feasibility of its application in real life, we further assemble all-solid-state portable ZAB configuration (Figures S18). As shown in Figure S19, the high OCV of 1.354 V for a single NiO/CoO TINWs-based portable ZAB was obtained at 25 ºC, with two portable ZABs integrated in-series can successfully illuminate a green LED under ambient conditions (Figures S20). More interestingly, even at the severe environment, such as -10 ºC or 80 ºC, the OCV of this portable ZAB with NiO/CoO TINWs as air-electrode displays little fluctuate and keep in the region of 1.33-1.37 V (Figure 3c). Figure 3d&e exhibit the specific capacities and energy densities trend of this NiO/CoO TINWs-driven portable ZAB with different temperature (-10 ºC, -5 ºC, 0 ºC, 10 ºC, 25 ºC, 35 ºC, 50 ºC, 65 ºC and 80 ºC), respectively. With 25 ºC as the best condition (specific capacity: 842.58 mAh $g_{Zn}^{-1}$ and energy density: 996.44 Wh $kg_{Zn}^{-1}$), this portable ZAB still possess high value of specific capacity (328.57 mAh $g_{Zn}^{-1}$)/energy density (364.45 Wh $kg_{Zn}^{-1}$) at subzero temperature (-10 ºC) and also high value of specific capacity (313.28 mAh $g_{Zn}^{-1}$)/energy density (341.35 Wh $kg_{Zn}^{-1}$) at corresponding-high temperature (80 ºC) (Figure S21&Table S5). Furthermore, this portable ZAB exhibits extremely long cycle life of more than 33 h, and

also the excellent stability even decreasing the temperature to -10 ºC or elevating to 80 ºC, which can still smoothly work at least 14 or 12 h, respectively (Figure 3f&Figure S22). All these data demonstrate this NiO/CoO TINWs-based portable battery possess excellent anti-freezing and heat-resistant property, further ensuring its potential for the practical application in a large temperature range.

Furthermore, we compare the free energy pathway among NiO (100), NiO (111), NiO (TI) and CoO (TI) to understand the OER reactivity (Figure 4a-c). At the U=0 V, the initial [*OH]-adsorption favours at the NiO (111) with an almost energetically adiabatic trend boosting the formation towards O*. All four systems demonstrate the potential determining step (PDS) at the formation of [$HOO^*+H_2O+OH^-$]. The energetic difference to form [$O_2$ (g)+*+$2H_2O$] at the last step is diversified (Figure 4a). For the U=1.23 V, the over-binding effect is noticed in NiO (111) systems rather than the TI region, which is consistent with electronic activity analysis (Figure 4b). We benchmarked the overpotentials as 0.58 V, 0.69 V, 1.07 V, and 1.28 V for CoO (TI), NiO (TI), NiO (111), and NiO (100), respectively (Figure 4c). The TI alleviates the barrier for both stabilizing HOO* and electron-transfer to achieve high reactivities. Further structural evolution displays that the electron-rich TI region can not only facilitate the initial facile O-H bond cleavage of H2O but also enhance the enhanced electron-negative O to further oxidize the HOO* (Figure 4d). The electronically active (111) surface regions will locally stabilize the H to prevent active sites covering. Meanwhile, the interfacial short-range disorder further minimizes the intermediating energetic cost with lattice relaxation, illustrating the vital function of TI region for optimal OER performance and energetically favourable ORR process.

In summary, well-defined NiO/CoO TINWs were fabricated via an oxygen removing/re-doping method. The as-synthesized NiO/CoO TINWs featured with abundant atomically-thinned transition interface were demonstrated as highly effective and stable air-cathode for OER and ORR. DFT calculations reveal that the interface system coordinational defects with high and low CNs with (111) and (100) lattice symmetry were maintained. Such a scenario uniquely preserves the co-existence of the high and low valence of Co-sites for fast redox rate with lower activation barrier. The interface not only possesses an electron-rich character but also contributes an effective electron-transfer site for stabilizing *OOH, which is the key element for optimally minimizing overall OER barriers, as well as the ORR process. The assembled portable ZABs with NiO/CoO TINWs as air-cathode exhibited high specific capacity of 842.58 mAh $g_{Zn}^{-1}$, large energy density of 996.44 Wh $kg_{Zn}^{-1}$ and long stability of 33 h at 25 ºC, which can also work at severe condition, such as subzero -10 ºC and high temperature of 80 ºC, rendering the portable ZABs operate properly in a wide temperature window.

## Acknowledgements

We acknowledge support from the National Natural Science Foundation of China (Nos. 21571089) and the Fundamental Research Funds for the Central Universities (lzujbky-2018-k08, lzujbky-2017-115, lzujbky-2018-19 it40). We thanks technical support from SMZ.

**Keywords:** transition interfaces • coordinational defects • $t_{2g}$-$e_g$ • wide temperature range • portable ZABs

[1] a) D. Larcher, J.-M. Tarascon, *Nat. Chem.* **2014**, *7*, 19-29; b) S. Sun, Y. Sun, Y. Zhou, S. Xi, X. Ren, B. Huang, H. Liao, L. P. Wang, Y. Du, Z. J. Xu, *Angew. Chem.* DOI:10.1002/ange.201902114; *Angew. Chem. Int. Ed.* DOI:10.1002/ anie.201902114.

[2] F. Meng, H. Zhong, D. Bao, J. Yan, X. Zhang, *J. Am. Chem. Soc.* **2016**, *138*, 10226-10231.

[3] Y. Zhang, B. Ouyang, J. Xu, G. Jia, S. Chen, R. S. Rawat, H. J. Fan, *Angew. Chem.* **2016**, *128*, 8812-8816; *Angew. Chem. Int. Ed.* **2016**, *55*, 8670-8674.

[4] C. Guo, Y. Zheng, J. Ran, F. Xie, M. Jaroniec, S.-Z. Qiao, *Angew. Chem.* **2017**, *129*, 8659-8663; *Angew. Chem. Int. Ed.* **2017**, *56*, 8539-8543;

[5] X. Gao, H. Zhang, Q. Li, X. Yu, Z. Hong, X. Zhang, C. Liang, Z. Lin, *Angew. Chem.* **2016**, *128*, 6398-6402; *Angew. Chem. Int. Ed.* **2016**, *55*, 6290-6294.

[6] A. L, X. Chang, Z. Huang, C. Li, Y. Wei, L. Zhang, T. Wang, J. Gong, *Angew. Chem.* **2016**, *128*, 13938-13942; *Angew. Chem. Int. Ed.* **2016**, *55*, 13734-13738.

[7] P.-C. Chen, M. Liu, J. S. Du, B. Meckes, S. Wang, H. Lin, V. P. Dravid, C. Wolverton, C. A. Mirkin, *Science* **2019**, *363*, 959-964.

[8] M. Lin, G.-H. Kim, J.-H. Kim, J.-W. Oh, J.-M. Nam, *J. Am. Chem. Soc.* **2017**, *139*, 10180-10183.

[9] C. W. Li, J. Ciston, M. W. Kanan, *Nature.* **2014**, *508*, 504-507.

[10] a) Y. Yao, Z. Huang, P. Xie, S. D. Lacey, R. J. Jacob, H. Xie, F. Chen, A. Nie, Pu. T, M, Rehwoldt, D. Yu, M. R. Zachariah, C. Wang, R. Shahbazian-Yassar, J. Li, L. Hu, *Science* **2018**, *359*, 1489-1494; b) J. L. Fenton, B. C. Steimle, R. E. Schaak, *Science* **2018**, *360*, 513-517.

[11] L. An, J. Feng, Y. Zhang, R. Wang, H. Wen, G. C. Wang, F. Cheng, X. Pin, *Adv. Funct. Mater.* **2019**, *29*, 1805298.

[12] a) J. Gao, L. Li, J. Tan, H. Sun, B. Li, J. C. Idrobo, C. V. Singh, T.-M. Lu, N. Koratkar, *Nano Lett.* **2016**, *16*, 3780-3787; b) X. Jiao, Z. Chen, X. Li, Y. Sun, S. Gao, W. Yan, C. Wang, Q. Zhang, Y. Lin, Y. Luo, Y. Xie, *J. Am. Chem. Soc.* **2017**, *139*, 7586-7594.

[13] K. He, S. Zhang, J. Li, X. Yu, Q. Meng1, Y. Zhu, E. Hu, Ke. S, H. Yun, X.-Q. Yang, Y. Zhu, H. Gan, Y. Mo, E. A. Stach, C. B. Murray, D. Su, *Nat. Commun.* **2016**, *7*, 11441.

[14] M. Saruyama, Y.-G. So, K. Kimoto, S. Taguchi, Y. Kanemitsu, T. Teranishi, *J. Am. Chem. Soc.* **2011**, *133*, 17598-17601.

[15] a) L. Karvonen, M. Valkeapaa, R.-S. Liu, J.-M. Chen, H. Yamauchi, M. Karppinen, *Chem. Mater.* **2010**, *22*, 70-76; b) J. R. Petrie, C. Mitra, H. Jeen, W. S. Choi, T. L. Meyer, F. A. Reboredo, J. W. Freeland, G. Eres, H. N. Lee, *Adv. Funct. Mater.* **2016**, *26*, 1564-1570.

[16] N. Zhang, X. Li, H. Ye, S. Chen, H. Ju, D. Liu, Y. Lin, W. Ye, C. Wang, Q. Xu, J. Zhu, L. Song, J. Jiang, Y. Xiong, *J. Am. Chem. Soc.* **2016**, *138*, 8928-8935.

[17] J. Bao, X. Zhang, B. Fan, J. Zhang, M. Zhou, W. Yang, X. Hu, H. Wang, B. Pan, Y. Xie, *Angew. Chem.* **201**5, *127*, 7507-7512; *Angew. Chem. Int. Ed.* **2015**, *54*, 7399-7404.

[18] J. C. Meier, I. Katsounaros, C. Galeano, H. J. Bongard, A. A. Topalov, A. Kostka, A. Karschin, F. Schüth, K. J. Mayrhofer, *Energy Environ. Sci.* **2012**, *5*, 9319-9330.

[19] Y. Jiao, Y. Zheng, M. Jaroniec, S.-Z. Qiao, *Chem. Soc. Rev.* **2015**, *44*, 2060-2086.

[20] J. Yin, Q. Fan, Y. Li, F. Cheng, P. Zhou, P. Xian, S. Sun, *J. Am. Chem. Soc.* **2016**, *138*, 14546-14549.

[21] a) N. Han, K. R. Yang, Z. Lu, Y. Li, W. Xu, T. Gao, Z. Cai, Y. Zhang, V. S. Batista, W. Liu, X. Sun, *Nat. Commun.* **2018**, *9*, 924; b) Y. Zhou, S. Sun, J. Song, S. Xi, B. Chen, Y. Du, A. C. Fisher, F. Cheng, X. Wang, H. Zhang, Z. J. Xu, *Adv. Mater.* **2018**, *30*, 1802912.

[22] X. Liu, M. Park, M. G. Kim, S. Gupta, G. Wu, J. Cho, *Angew. Chem.* **2015**, *127*, 9790-9794; *Angew. Chem. Int. Ed.* **2015**, *54*, 9654-9658.

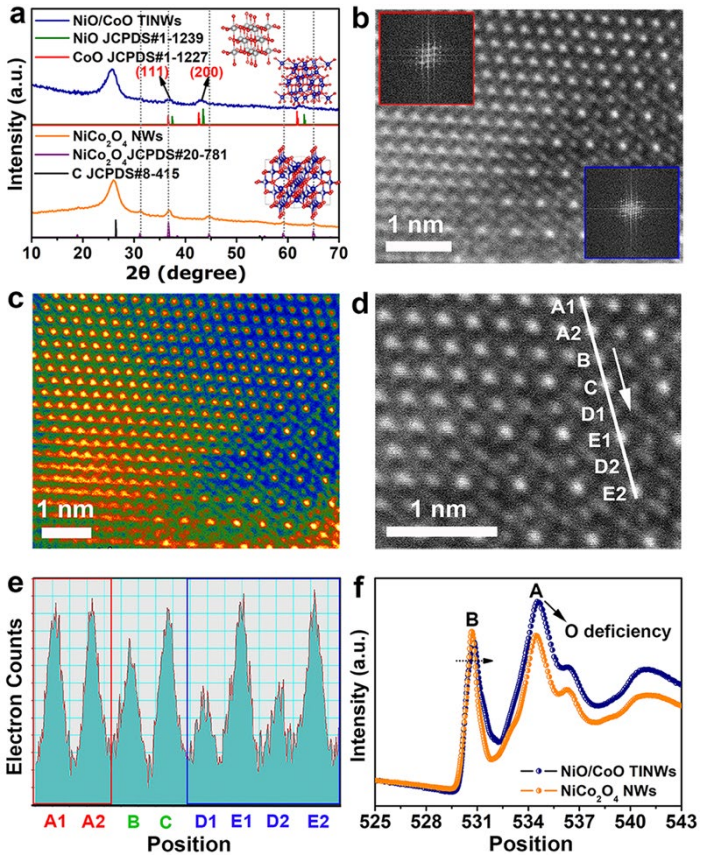


**Figure 1.** a) XRD patterns of NiO/CoO TINWs and $NiCo_2O_4$ NWs. b) Atomic-resolution HAADF-STEM image of NiO/CoO TINWs, along with their respective Fast Fourier Transforms (*inset*). c) FFT-filtered atomic resolution image using two sets of diffraction spots. d) The magnified atomic-resolution HAADF-STEM image of NiO/CoO TINWs. e) Intensity profile across the interface, corresponding to the white line in (d). f) The O-K edge XANES spectra of NiO/CoO TINWs and $NiCo_2O_4$ NWs.

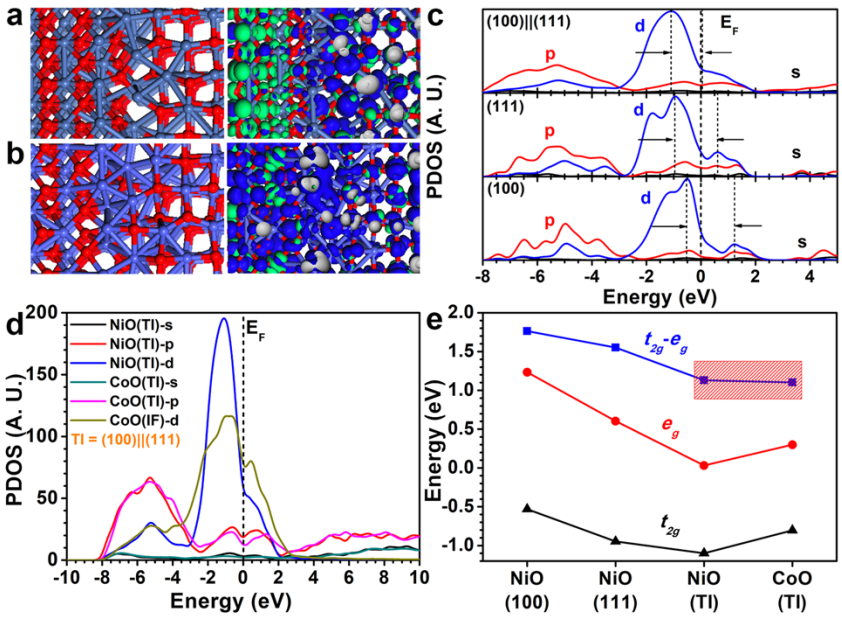

**Figure 2.** a) The top-views of NiO (TI) (*left*-panel) and the real-spatial contour plots for the bonding and anti-bonding orbitals near the $E_F$ of the bonding-form TI model (*right*-panel). b) The top-views of CoO (TI) (*left*-panel) and the real-spatial contour plots for the bonding and anti-bonding orbitals near the $E_F$ of the bonding-form TI model (*right*-panel). c) The comparison of the PDOSs for NiO (TI), NiO (111) and NiO (100) systems. d) The PDOSs comparisons between NiO (TI) and CoO (TI) systems. e) The summarized $t_{2g}$ and $e_g$ splitting trends for NiO (100), NiO (111), NiO (TI) and CoO (TI), respectively

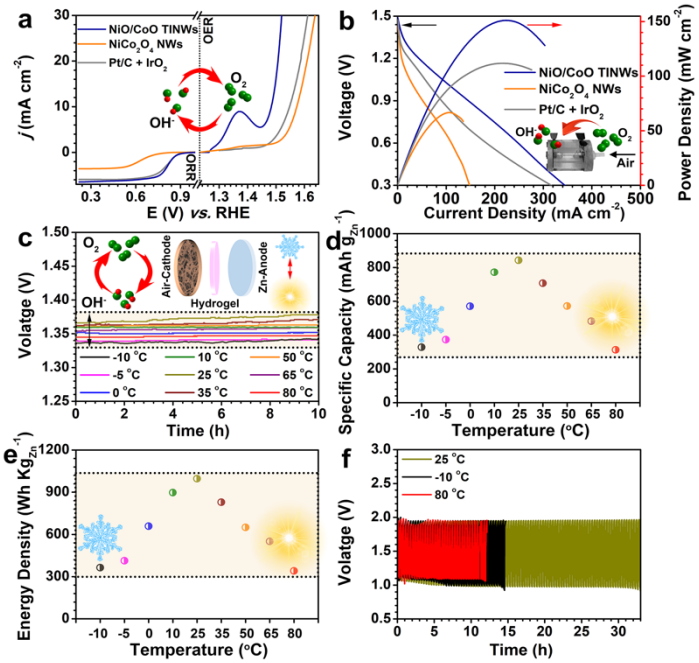


**Figure 3.** a) The overall polarization curves of these catalysts within the OER and ORR potential window. d) The polarization and power density curves of primary ZABs with these catalysts as air-cathodes. c) The open-circuit plot of NiO/CoO TINWs at different temperature tested in portable ZABs. d) The specific capacities and e) energy densities trend with temperature. f) Long-term charge/discharge cycling tests of the portable ZABs with NiO/CoO TINWs as air-cathode at the current density of 1 mA $cm^{-2}$ under different temperature.

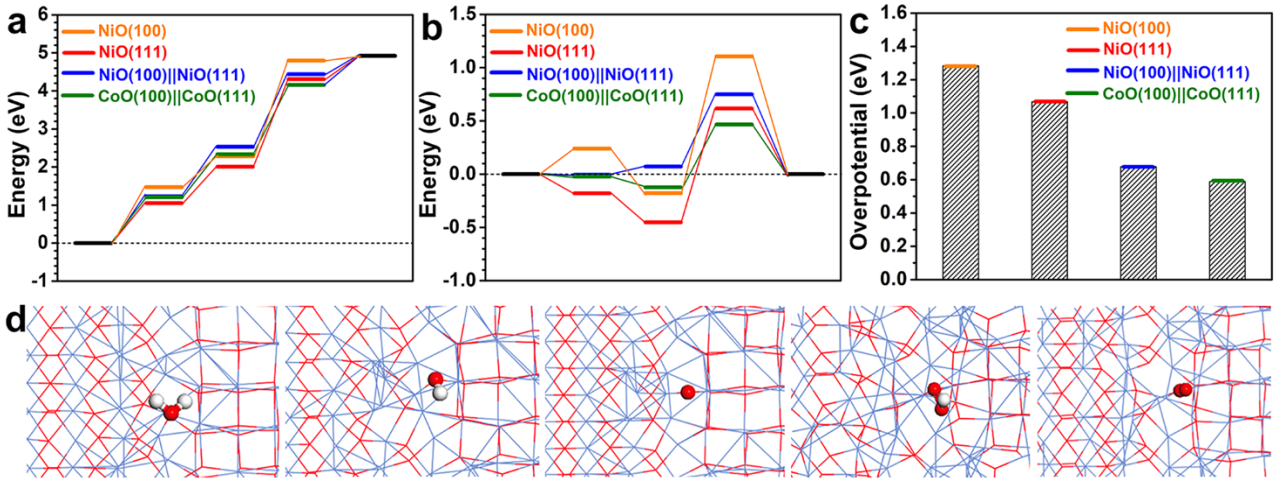


**Figure 4.** a) Reaction energetic pathways for catalytic OER among NiO (100), NiO (111), NiO (TI) and CoO (TI) systems at U=0 V electrode potential. b) OER pathways under U=1.23 V potential. c) Overpotential benchmarks among NiO (100), NiO (111), NiO (TI) and CoO (TI) systems. d) The evolutions of local structural configurations for illustrating the OER process from TI region within the NiO (TI) system, where the red ball denotes for O and white ball denotes for H.

# COMMUNICATION

The NiO/CoO transition interfacial nanowires (TINWs) with abundant interfacial coordinational coupled defects were obtained during the oxygen removing and re-doping process. The atomic-thick transition interface renders NiO/CoO TINWs as highly efficient and stable bifunctional OER/ORR catalyst, and also enable the wide operation temperature working range (-10 ºC~80 ºC) for portable ZABs.

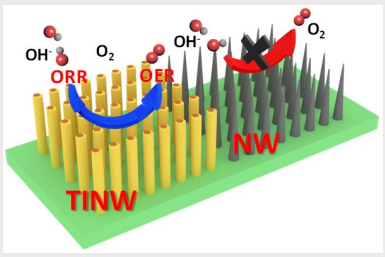


*Li An, Bolong Huang, Yu Zhang, Rui Wang, Nan Zhang, Tengyuan Dai, Hong Zhang, Pinxian Xi* and Chun-Hua Yan**

***Page No. – Page No.***

**Transition Coordinational Coupled Interfaces-Promoted Portable Zn-Air Battery Working in Wide Temperature Range**